

On Characterization of Flow Disturbances in Arc-Jet Testing

Tahir Gökçen¹

AMA Inc., NASA Ames Research Center, Moffett Field, CA 94035

This paper reports computational simulations and analysis of flow characterization tests in high enthalpy arc-jet facilities at NASA Ames Research Center. Flow disturbances and their characterization are presented through case studies, and their implications for testing are discussed. The case studies include free-jet test configurations from three different arc heaters and nozzles: the 60-MW IHF 30-inch conical nozzle, the 10-MW TP3 15-inch conical nozzle, and the 20-MW AHF 12-inch conical nozzle. For all cases, test articles are placed in the jet exiting the conical nozzle, and the existence of a flow disturbance is confirmed through flow survey data using pitot pressure and heat flux probes and accompanying analysis. The paper focuses on cases where the effects of the disturbances on test article surface quantities are important. The present analysis comprises computational fluid dynamics simulations of the nonequilibrium flowfield in the facility nozzles and test box, including the models tested. Comparisons of computations with the experimental measurements are presented. The computations that reproduce the probe sweep data approximately are essential to interpret the arc-jet test data accurately, while providing insights into several observed calorimeter anomalies caused by flow disturbances.

I. Nomenclature

c_i	= species mass fraction for species i
D_e	= nozzle exit diameter, cm (or in)
h	= enthalpy, MJ/kg
h_o	= total enthalpy, MJ/kg
h_{ob}	= mass-averaged total enthalpy (or bulk enthalpy), MJ/kg
h_{oc1}	= centerline total enthalpy, MJ/kg
I	= arc current, A
M	= Mach number
\dot{m}	= total mass flow rate, g/s
\dot{m}_m	= arc heater main air flow rate, g/s
\dot{m}_a	= add-air flow rate or cold-gas injection rate at the plenum (N_2), g/s
\dot{m}_{ar}	= argon flow rate, g/s
\dot{m}_{N_2}	= nitrogen flow rate, g/s
\dot{m}_{O_2}	= oxygen flow rate, g/s
p	= pressure, kPa
p_{box}	= test box pressure, torr
p_{ch}	= arc-heater pressure, kPa
p_{midc}	= arc-heater mid-column pressure, kPa
p_o	= total pressure, kPa
p_{t2}	= pitot pressure or model stagnation pressure, kPa
q_{CG}	= heat flux from a 10.16-cm hemisphere probe with a coaxial thermocouple, W/cm^2
q_{ffc8}	= heat flux from a 20.32-cm flat-faced slug calorimeter ($r_c=0.95$ cm), W/cm^2
q_{GG}	= heat flux from a 1.59-cm hemisphere Gardon-gage probe, W/cm^2
q_{hemi}	= heat flux from a 10.16-cm hemisphere slug calorimeter, W/cm^2
q_{isoq}	= heat flux from a 10.16-cm iso-q slug calorimeter, W/cm^2
q_{RCG}	= hot-wall heat flux computed using RCG surface kinetics, W/cm^2
q_s	= surface heat flux, W/cm^2

¹ Senior Research Scientist, MS 230-2, Associate Fellow AIAA

r_c	=	model corner radius, cm
r_n	=	nose radius, cm
s	=	arc-length coordinate or the survey probe location, m
T	=	temperature or translational-rotational temperature, K
T_v	=	vibrational-electronic temperature, K
V	=	arc voltage, V
x_{ml}	=	model location from the nozzle exit plane, cm
ε	=	hemispherical emissivity, 0.89

II. Introduction

Arc-jet facilities provide the primary means to study the performance of various types of thermal protection systems (TPS) in an aerothermodynamic heating environment. In a high enthalpy arc-jet facility, a test gas, usually air-argon mixture or a mixture of nitrogen and oxygen, is passed through an electric arc discharge where the energy is added to the flow. The test gas is then expanded through a converging-diverging nozzle into an evacuated test chamber to produce high-enthalpy supersonic or hypersonic flow. NASA Ames Research Center (ARC) has four arc-jet facilities within its Arc-Jet Complex [1]. The present paper reports computational simulations and analysis of flow characterization tests from three different arc heaters and nozzles: the 60-MW Interaction Heating Facility (IHF) with the 30-inch diameter conical nozzle [1, 2], the 10-MW TP3 heater in the Aerodynamic Heating Facility (AHF) with the 15-inch conical nozzle [3-5], and the 20-MW heater in the AHF with the 12-inch conical nozzle [1].

The primary objective of the paper is to present three case studies involving flow disturbances. For each case, characterization of the flow disturbance is presented. The existence of a flow disturbance is determined using pitot pressure and heat flux probe sweeps and accompanying analysis based on CFD simulations. Although the original source of these disturbances is often not known precisely, for some cases their origin can be traced back to the nozzle throat region or locations near the nozzle joints. These disturbances alter the flowfield over the test articles. As a result, they affect model surface pressure and heat flux values and their distributions. One recent example of a flow disturbance observed in the IHF 9-inch nozzle flow has been reported in [6]. The present analysis comprises CFD simulations of the nonequilibrium flowfield in the facility nozzle and test box, including the models tested. Comparisons of CFD results with the experimental measurements are presented. Through CFD analysis, effects of the flow disturbances on the model surface quantities are assessed, and their implications for arc-jet testing are discussed.

III. Arc-Jet Facilities and Tests

The arc-jet facilities and tests considered are briefly described here.

The IHF is designed to operate with a set of conical nozzles or two semi-elliptical nozzles at total pressures of 1-9 atm and total bulk enthalpies of 2-28 MJ/kg (air) [1, 2]. The 60-MW constricted arc heater produces high-temperature test gas for both nozzle configurations. The IHF 30-inch conical nozzle, like the other IHF conical nozzles, has a throat diameter of 6.033 cm (2.375 in) and the same 10° half-angle for the diverging section, and it has an exit diameter of 76.2 cm (30 in). The probe survey data in the IHF 30-inch conical nozzle were obtained during IHF 329 test series in 2017. The surveys of the nozzle jet in the test section were performed with two probes: a 10.16-cm hemisphere calorimeter with a coaxial thermocouple gage and a 15° sphere-cone probe ($r_n = 6.35$ mm or 0.25 in), or the 12.7-mm diameter sphere-cone probe. For these surveys, the probes do not move horizontally or vertically across the jet, but rather follow an arc path with a radius of 139.7 cm (since they are attached to a swing arm). For each survey, first, they move in a forward sweep passing through the nozzle centerline, then they retract back in a backward sweep. Further information on the survey probes can be found in [7]. For IHF 329 tests, the test articles used were 10°-yawed wedge models designed by David A. Stewart of NASA ARC. The wedge cross section has 15° half-angle with a radius of 5.08 cm. The wedge model has nose radius of 5.08 cm at the leading edge, with blending into the wedge section.

The AHF, with its 10-MW TP3 constricted arc-heater configuration, is designed to operate with a set of conical nozzles. The TP3 15-inch conical nozzle has an inlet diameter of 10.16 cm (4 in), a throat diameter of 5.715 cm (2.25 in), and an exit diameter of 38.1 cm (15 in). The diverging section of each nozzle has a half-angle of 15° [5]. The probe survey data in the TP3 15-inch conical nozzle were obtained during AHF 341 test series in 2019, and they were reported in [5]. The pitot pressure and Gardon-gage heat flux surveys of the nozzle jet in the test section were

performed using 1.59-cm diameter hemisphere probes ($D=0.625$ in). Two survey probes were used: one with a stagnation-point pressure port, the other with a Gardon heat flux gage. The sweeps to survey across the nozzle were done by moving the probes horizontally across the free jet in two directions: first from east to west, then retracting back west to east. Each condition was calibrated separately for its centerline conditions with 20.32-cm diameter flat-faced slug calorimeters (the same shape as the test articles used, $r_c=0.95$ cm). Also, 10.16-cm diameter iso-q slug calorimeter measurements were used to check for consistency and establish repeatability of these conditions. Figure 1 shows a schematic diagram of a wall-constricted arc-jet with its interchangeable nozzles and a photograph of a flat-faced model test in the TP3 15-inch nozzle.

The AHF, with its 20-MW constricted arc-heater configuration, is also designed to operate with a set of conical nozzles. The AHF 12-inch conical nozzle has an inlet diameter of 12.07 cm (4.75 in), a throat diameter of 3.81 cm (1.5 in), and an exit diameter of 30.48 cm (12 in). The diverging section of each nozzle has a half-angle of 8° . The probe survey data in the AHF 12-inch conical nozzle were obtained during AHF 345 test series in 2021. The survey probes were the same pitot pressure and heat flux probes used in AHF 341 tests, the 1.59-cm diameter hemisphere probes. The arc-jet conditions were calibrated using 15.24-cm diameter flat-faced and 10.16-cm diameter iso-q slug calorimeters.

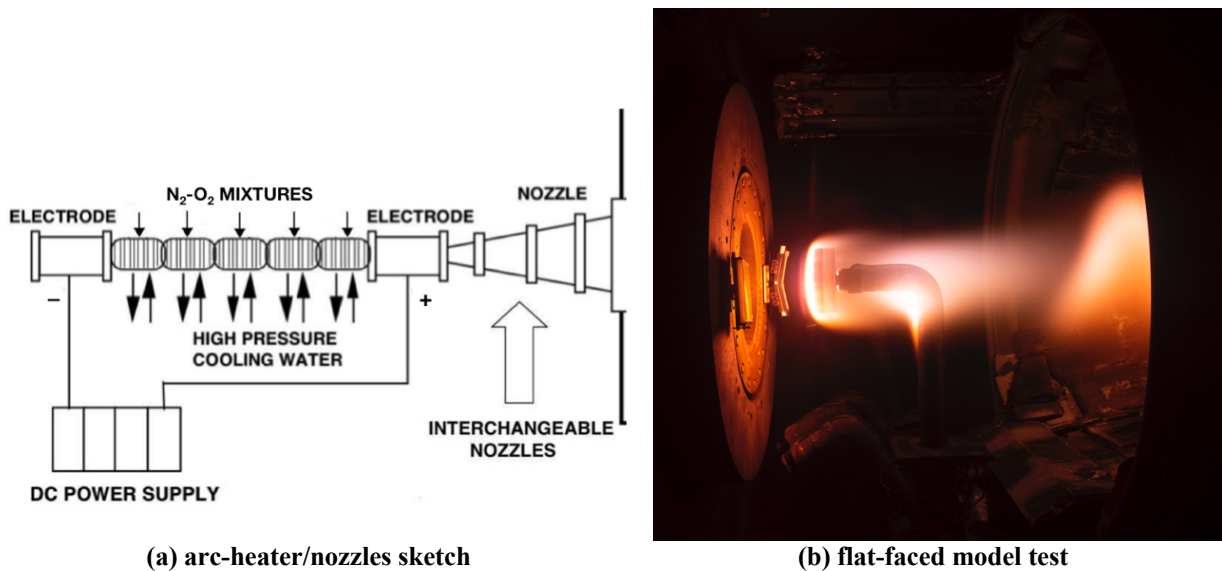


Figure 1. TP3 sketch and a photograph of TP3 15-inch nozzle test.

Figure 2 shows photographs of the 1.59-cm hemisphere pitot probe and Gardon gage calorimeter used for the flow surveys in the TP3 15-inch and AHF 12-inch nozzles, or in the AHF 341 and AHF 345 tests, respectively.



Figure 2. Photographs of the 1.59-cm hemisphere pitot probe and Gardon gage calorimeter used for the flow surveys in the TP3 15-inch and AHF 12-inch nozzles.

Table 1. Summary of arc-jet facility conditions, slug calorimeter data, and CFD enthalpy estimates.

60-MW IHF, 30-inch nozzle	IHF 329, condition 6 (Runs 6–10), IHF 3030 Run 3-6
p_{ch} , kPa	366
I , A	3829
V , V	4170
\dot{m} , g/s	410
\dot{m}_m , g/s	323
\dot{m}_a , g/s	58
\dot{m}_{ar} , g/s	29
$x_{ml} = 25.4$ cm, q_{hemi} , W/cm ²	235
p_{hemi} , kPa	4.2
CFD, h_{ob} , MJ/kg	15.9
CFD, h_{ocl} , MJ/kg	17.8
10-MW TP3, 15-inch nozzle	AHF 341, condition 2 (Runs 4-3, 13-2, and 29-2)
p_{midc} , kPa	522
I , A	1756
V , V	4861
\dot{m} , g/s	500
\dot{m}_{N_2}	385
\dot{m}_{O_2}	115
$\dot{m}_{a(N_2)}$	0
$x_{ml} = 20.3$ cm, q_{ffc8} , W/cm ²	180
p_{ffc8} , kPa	10.2
CFD, h_{ob} , MJ/kg	12.9
CFD, h_{ocl} , MJ/kg	28.8
20-MW AHF, 12-inch nozzle	AHF 345, condition 2 (Runs 17–20), FCO Runs 130–139
p_{ch} , kPa	431
I , A	1517
V , V	3678
\dot{m} , g/s	185
\dot{m}_m , g/s	170
\dot{m}_a , g/s	0
\dot{m}_{ar}	15
$x_{ml} = 10.2$ cm, q_{isoq} , W/cm ²	283
p_{isoq} , kPa	10.9
$x_{ml} = 15.2$ cm, q_{isoq} , W/cm ²	354
p_{isoq} , kPa	10.6
$x_{ml} = 34.3$ cm, q_{isoq} , W/cm ²	189
p_{isoq} , kPa	7.0
CFD, h_{ob} , MJ/kg	16.9
CFD, h_{ocl} , MJ/kg	16.9

Note that the facility and slug calorimeter data for each case are averaged values from multiple runs. For AHF 345, 10.2-cm iso-q calorimeter measurements at $x_{ml} = 15.2$ cm and $x_{ml} = 34.3$ cm locations are single measurements.

IV. Computational Approach

Computational analyses of arc-jet tests are performed through simulation of nonequilibrium expanding flow in the arc-jet nozzle and supersonic jet, and simulation of the flow in the test box and around the test articles. For all CFD calculations, the Data Parallel Line Relaxation (DPLR) code [8, 9], a NASA Ames in-house flow solver, is used. DPLR provides various options for thermophysical models and formulation. For CFD calculations presented here, two-dimensional axisymmetric or three-dimensional Navier-Stokes equations, supplemented with the equations accounting for nonequilibrium kinetic processes, are used in the formulation. The thermochemical model employed for the arc-jet flow includes five species (N_2 , O_2 , NO , N , O), or six species (N_2 , O_2 , NO , N , O , Ar) when argon is present, and the thermal state of the gas is described by two temperatures (translational-rotational and vibrational-electronic) within the framework of Park's two-temperature model [10].

The flowfield in an arc-jet facility, from the arc heater to the test section, is a very complex, three-dimensional flow with various nonequilibrium processes occurring. To simulate the flowfield, several simplifying assumptions are made, and corresponding numerical boundary conditions are prescribed for CFD simulations. The present computational approach follows our earlier work [5, 11-14], and it is also briefly described here. Simulations of the arc-jet facility flow are started from the nozzle inlet. The total enthalpy and its radial profile at the inlet are prescribed based on the facility and calibration data, and the flow properties at the inlet are assumed to be in thermochemical equilibrium. Measured facility data, namely the total pressure, mass flow rate, and test box pressure, are used as boundary conditions.

V. Presentation of Results

Three case studies from the IHF 30-inch nozzle, TP3 15-inch nozzle and AHF 12-inch nozzle tests are presented. A summary of the facility parameters, slug calorimeter data, and CFD-estimated enthalpies for the three cases is given in Table 1.

A. IHF 30-inch nozzle tests (IHF 329)

For this case, existence of a flow disturbance in the IHF 30-inch nozzle was not known prior to this test series. Pre-test CFD simulations of the nozzle and test box did not show any potential flow disturbance originating from the nozzle throat region.

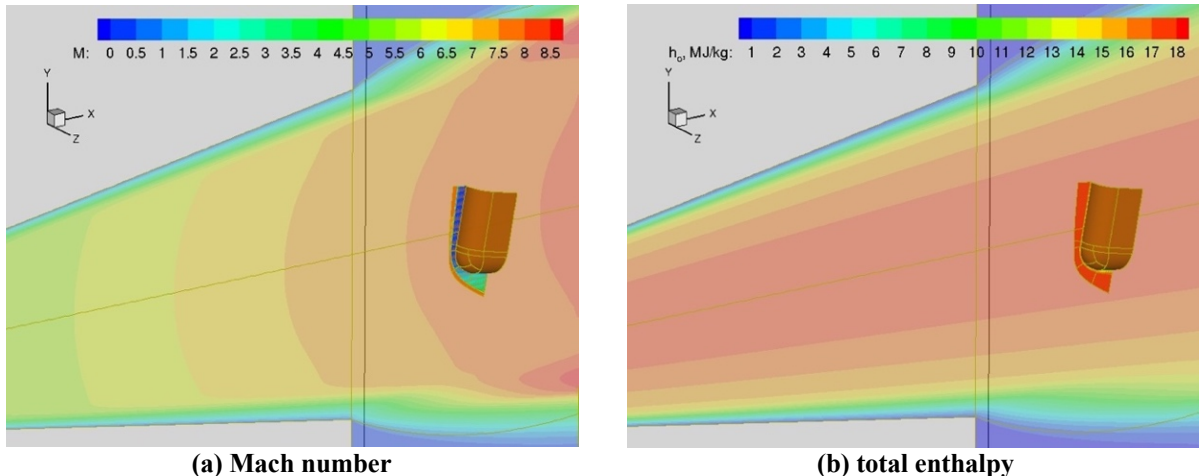


Figure 3. Computed flowfield contours of the IHF 30-inch nozzle flow and test box with the 10°-yawed wedge model (15° wedge angle) at $x_{nl} = 25.4$ cm location: $\dot{m} = 410$ g/s, $h_{ob} = 15.9$ MJ/kg, $h_{oc1} = 17.8$ MJ/kg, parabolic enthalpy profile, air with 7.1% Ar, $p_{box} = 0.1$ torr.

Figure 3 shows the computed Mach number and total enthalpy contours of the IHF 30-inch nozzle flow near the nozzle exit and test box with the 10°-yawed wedge model. The contours are shown on the x-y symmetry planes of the nozzle flowfield, including the test box and flowfield over the model. The wedge model was tested at 25.4 cm

downstream of the nozzle exit and at an off-centerline location (the leading edge of the model is about 5.1 cm below the centerline). Note that the computed Mach number contours in Fig. 3a do not indicate any presence of a flow disturbance. However, the probe sweeps conducted during the test program indicated a potential flow disturbance near the centerline.

Figure 4 shows comparisons of computations with the data from the pitot pressure and heat flux survey probes. Both pitot pressure and heat flux data show a feature near the nozzle centerline, showing higher pressure and heating levels. Although both pitot pressure and heat flux data are not exactly symmetric, they are repeatable within the measurement fluctuations between forward and backward sweep directions (FW and BW). CFD-predicted pitot pressure and heat flux distributions are in reasonable agreement with the survey data except near the nozzle centerline. This feature in the measured survey data is not ambiguous, so it can only be explained by the presence of a flow disturbance somewhere in the nozzle.

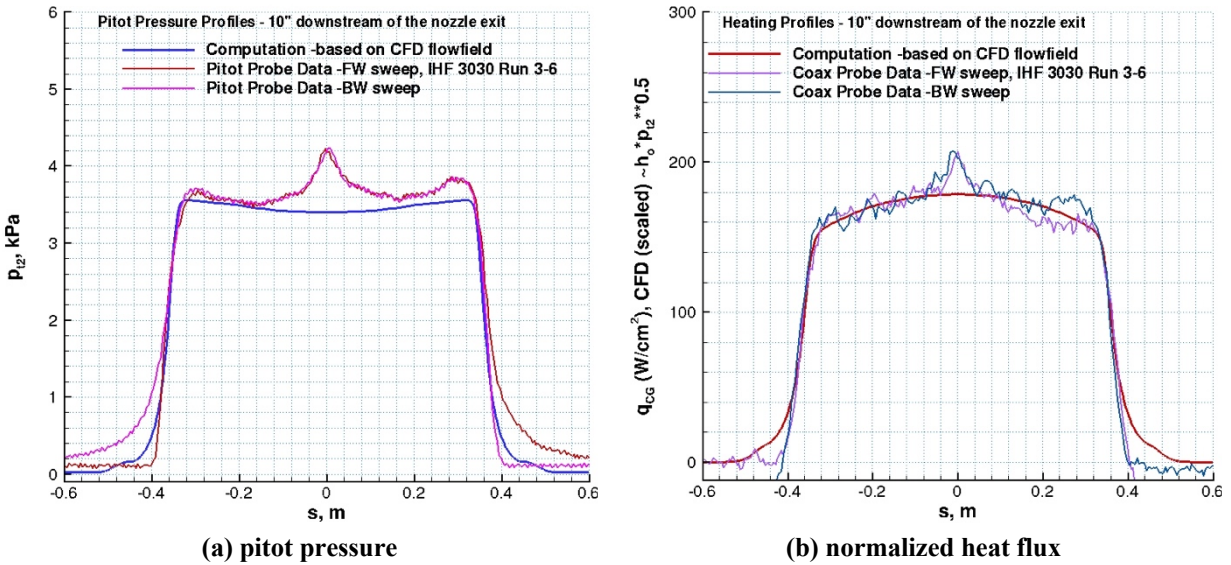


Figure 4. Comparisons of computations with the pitot pressure and heat flux survey data at $x_{ml} = 25.4$ cm location. IHF 30-inch nozzle flow: $\dot{m} = 410$ g/s, $h_{ob} = 15.9$ MJ/kg, $h_{oc1} = 17.8$ MJ/kg, parabolic enthalpy profile, air with 7.1% Ar, $p_{box} = 0.1$ torr.

In order to reproduce the measured survey data with CFD simulations, a flow disturbance in the nozzle (a small protuberance placed near one of the nozzle joints) is introduced. The original source of this disturbance is not known. The objective here is that if the survey data can be somehow reproduced with computations, one can investigate the effects of the disturbance on the model surface quantities. Figure 5 shows computed Mach number contours of the nozzle flow and test box, and comparisons of computations that included the flow disturbance with the pitot pressure and heat flux survey data. On the Mach number contour plot, the axial location of the probe surveys is indicated. The introduced flow disturbance starts at about 0.8 m downstream of the throat as a compression wave and propagates downstream. Note that the pitot pressure survey data are now reproduced well with these CFD simulations in Fig. 5b. Although the heat flux distribution is qualitatively reproduced by the CFD simulations in Fig. 5c, comparison of the normalized heat flux distributions indicates that the heating augmentation at the nozzle centerline is not exactly proportional to $h_o p_{t2}^{0.5}$ when there is a flow disturbance.

As mentioned earlier, effects of the flow disturbance on the model surface quantities are of interest for interpretation of the test data. Figure 6 shows the computed Mach number and total enthalpy contours of the IHF 30-inch nozzle flow near the nozzle exit and test box with the 10° -yawed wedge model, with the flow disturbance in the nozzle. Note that the Mach number contours shown in Fig. 6a are three dimensional CFD simulation results while those shown in Fig. 5a are axisymmetric results. The locations at which the flow disturbance impinges with the model shock wave are seen in Fig. 6a. Since the leading edge of the model is 5.1 cm below the nozzle centerline, the flowfield near the nose section of the model is not significantly affected.

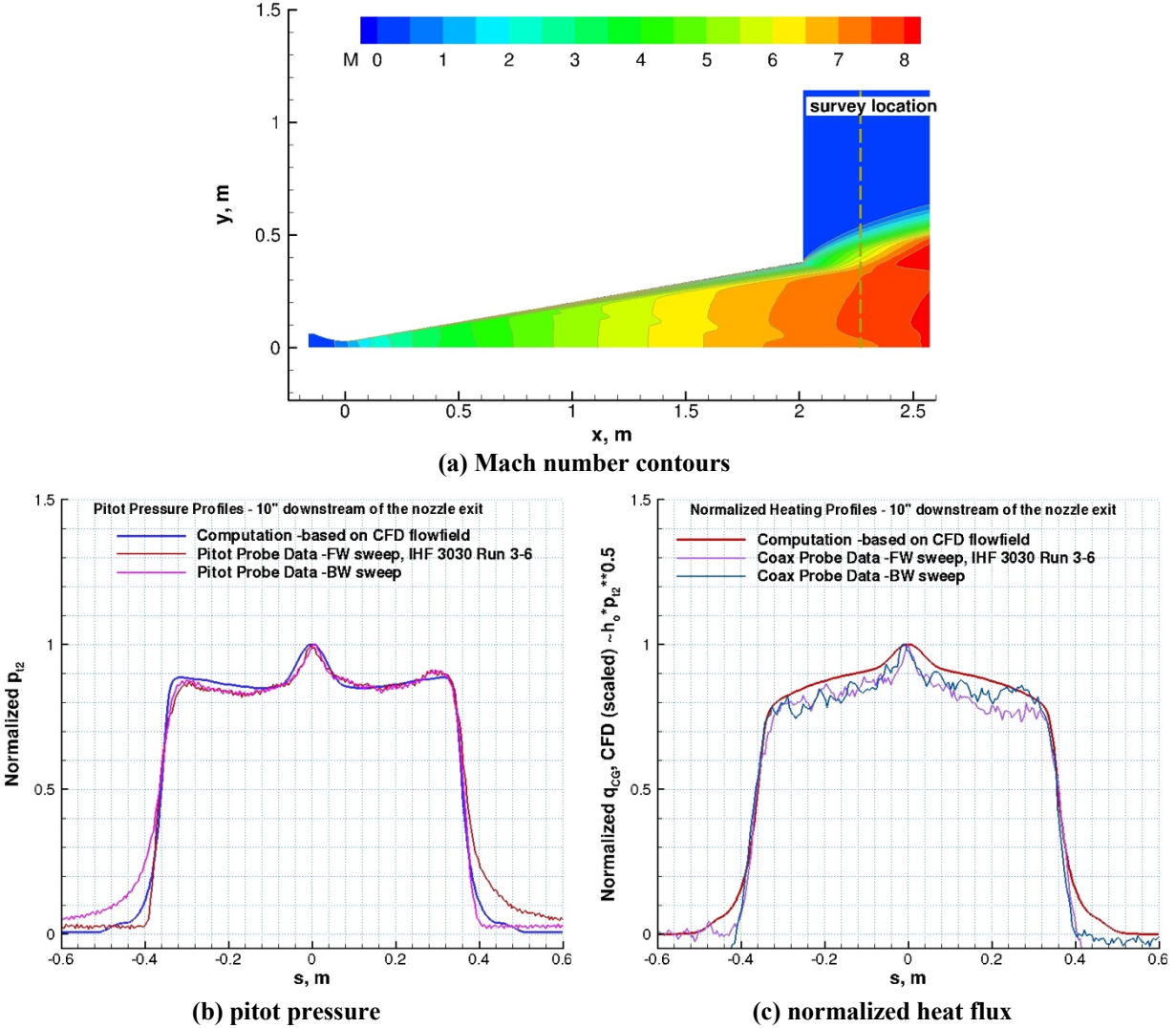


Figure 5. Computed Mach number contours and comparisons of computations including a flow disturbance with the pitot pressure and heat flux survey data at $x_{ml} = 25.4$ cm location. IHF 30-inch nozzle flow: $\dot{m} = 410$ g/s, $h_{ob} = 15.9$ MJ/kg, $h_{oct} = 17.8$ MJ/kg, parabolic enthalpy profile, air with 7.1% Ar, $p_{box} = 0.1$ torr.

Figure 7 shows computed surface heat flux contours and symmetry plane profiles of the RCG-coated 10° -yawed wedge model for two cases, the nominal case and the other with the flow disturbance in the CFD simulations. On the line plots of surface heat flux in Fig. 7a and 7b, the symmetry plane model geometry (the pale green curve) is also drawn to make interpretation of the plots easier. For the RCG-coated surfaces, surface catalytic efficiency expressions developed by Stewart [15] are prescribed, and surface temperatures and heat fluxes are calculated using the radiative equilibrium boundary condition ($\varepsilon = 0.89$). Although the predicted surface heat fluxes at the stagnation point are similar (about 82 W/cm² in both Fig. 7a and 7b) primarily due to the interaction location, there are differences in these two heat flux distributions. For the nominal case in Fig. 7a, computed heat flux decreases monotonically away from the stagnation point, and it drops to about 64 W/cm² at $y=0$ location on the symmetry plane. When the flow disturbance is included in CFD simulations (Fig. 7b), the computed heat flux does not decrease monotonically, and it is about 70 W/cm² at the same $y=0$ location. It should be mentioned here that there were a couple of experimental observations from IHF 329 tests with the 10° -yawed wedge model: (1) the temperature or heat flux difference between the stagnation-point and $y=0$ location was relatively small (30-50 K, pyrometer measurements); (2) non-monotonic temperature distribution from the stagnation point to $y=0$ location (infrared camera data). The CFD simulations with the flow disturbance that reproduce the survey data reasonably well provide a plausible explanation for these observations. As can be expected, the presence of the flow disturbance also affects colorimeter heat flux and pressure measurements, and their interpretation, which is addressed in the next two sections.

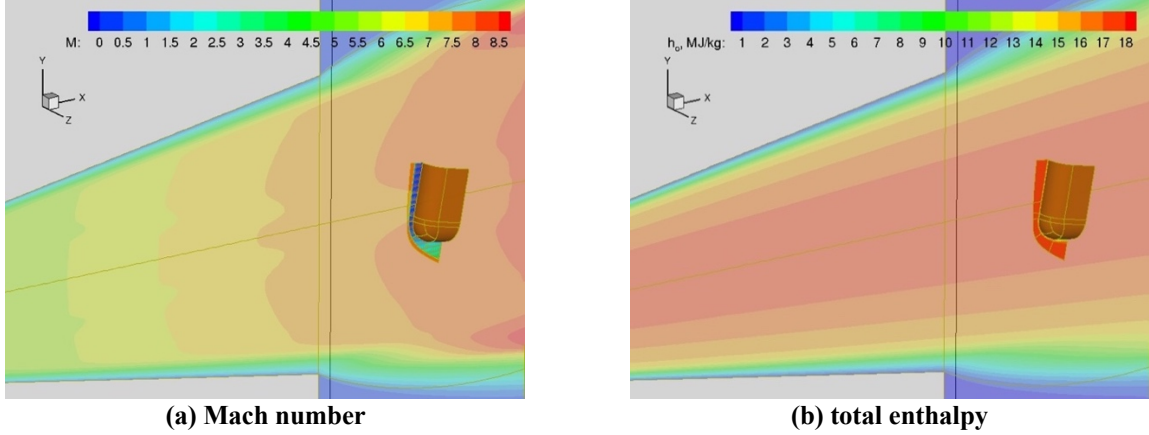


Figure 6. Computed flowfield contours of the IHF 30-inch nozzle flow and test box with the 10°-yawed wedge model with the flow disturbance: $\dot{m} = 410$ g/s, $h_{ob} = 15.9$ MJ/kg, $h_{ocl} = 17.8$ MJ/kg, parabolic enthalpy profile, air with 7.1% Ar, $p_{box} = 0.1$ torr.

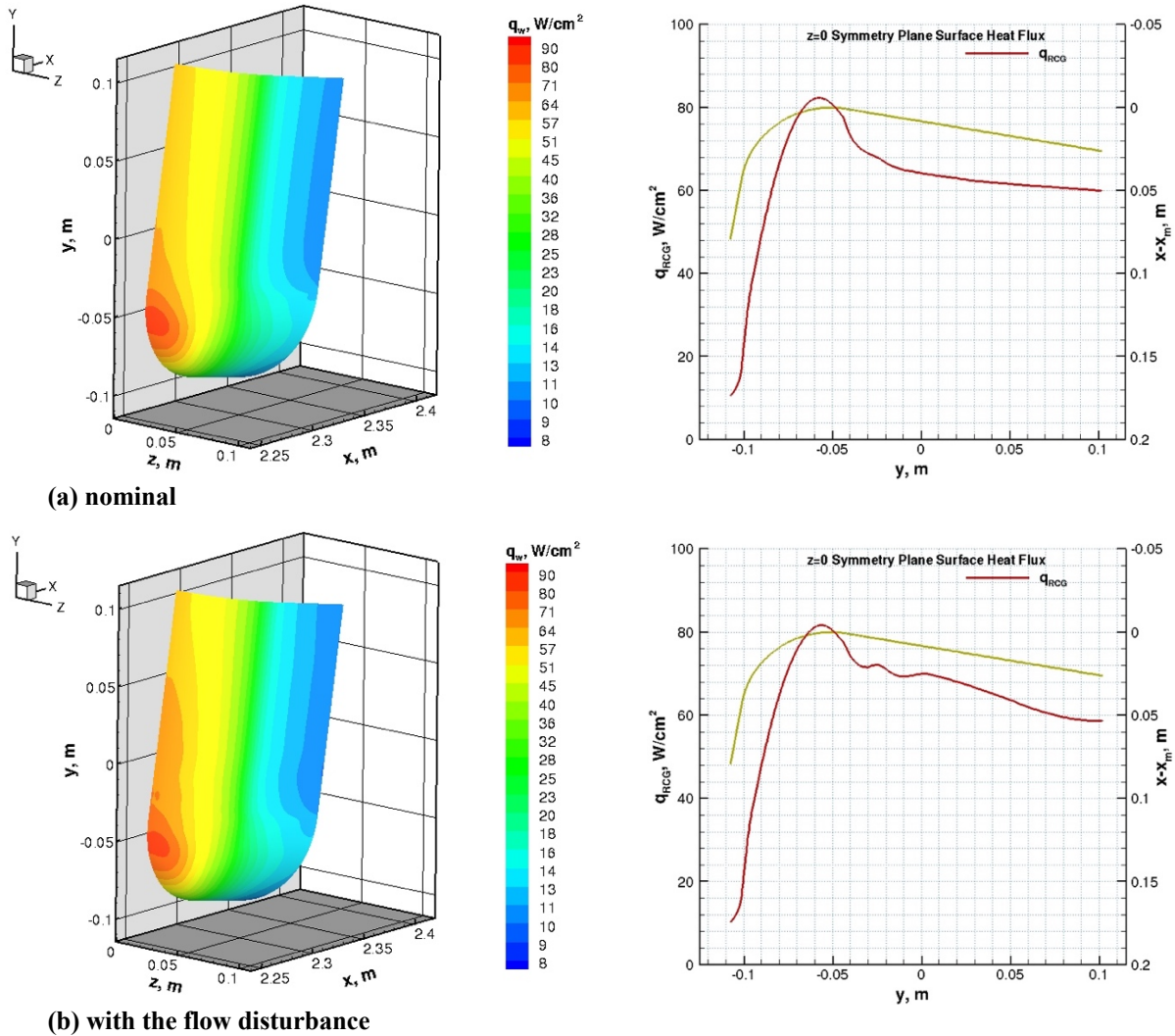
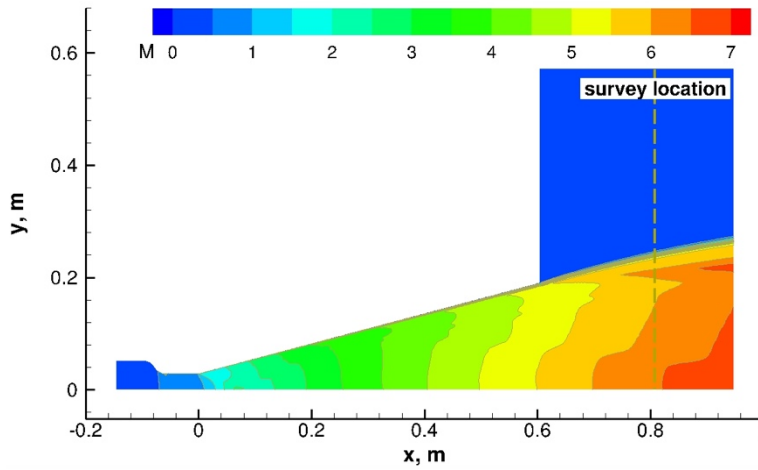


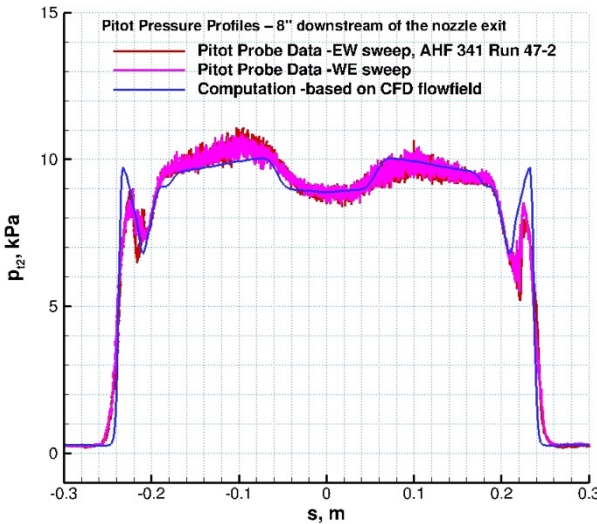
Figure 7. Computed surface heat flux contours and symmetry plane profiles of the RCG-coated 10°-yawed wedge model at $x_{ml} = 25.4$ cm. IHF 30-inch nozzle flow, nominal and with the flow disturbance: $\dot{m} = 410$ g/s, $h_{ob} = 15.9$ MJ/kg, $h_{ocl} = 17.8$ MJ/kg, parabolic enthalpy profile, air with 7.1% Ar, $p_{box} = 0.1$ torr.

B. TP3 15-inch nozzle tests (AHF 341)

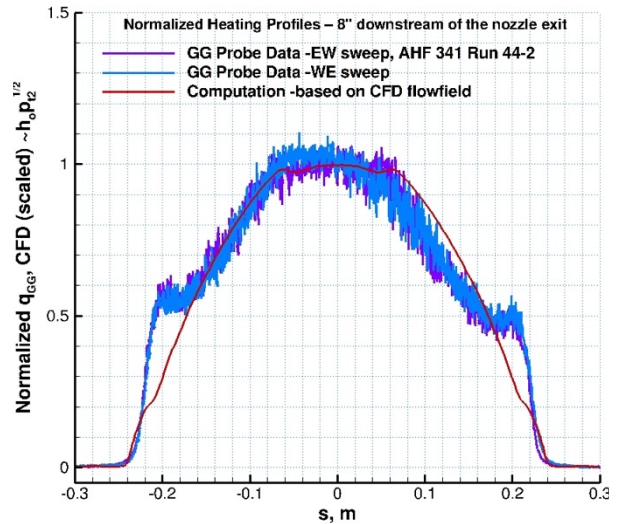
For this case, a flow disturbance in the nozzle and test box is predicted from both CFD simulations and probe survey data [5]. Figure 8 shows computed Mach number contours of the nozzle flow and test box, and comparisons of computations with the pitot pressure and Gardon-gage heat flux probe survey data. On the Mach number contour plot, location of the probe surveys is indicated, the axial location being approximately at $x = 0.806$ m or at $x_{ml} = 20.3$ cm. Both pitot pressure and heat flux data are repeatable within the measurement fluctuations between both sweep directions (EW and WE), and they are slightly asymmetric with respect to the nozzle/jet centerline. CFD simulations reproduce the pitot pressure and heat flux data reasonably well. Note that the measured pitot pressure profile, as well as the computations, both show a dip near the jet centerline. This non-uniform flow feature in the pitot pressure profile is an indication of a flow disturbance, and the origin of the disturbance can be traced back to the nozzle throat region [5]. The TP3 uses an elongated throat design (see Fig. 8a). As presented in [5], expansion waves are generated at the throat and diverging-nozzle cone intersection, and these expansion waves propagate downstream and reflect on the nozzle centerline as compression waves (at about $x = 0.1$ m in Fig. 8a), and then eventual shock formation. The oblique shock wave reflects from the nozzle wall at about $x = 0.28$ m in Fig. 8a.



(a) Mach number contours



(b) pitot pressure



(c) normalized heat flux

Figure 8. Computed Mach number contours and comparisons of computations with the pitot pressure and heat flux survey data at $x_{ml} = 20.3$ cm location. TP3 15-inch nozzle flow: $\dot{m} = 500$ g/s, $h_{ob} = 12.9$ MJ/kg, $h_{ocl} = 28.8$ MJ/kg, parabolic enthalpy profile, N_2/O_2 mixture, $p_{box} = 2$ torr.

A detailed discussion of the oblique shock formation in the 15-inch nozzle is given in [5]. It should also be mentioned here that the flow at this condition is highly non-uniform since the estimated centerline-to-bulk enthalpy ratio is about 2.23.

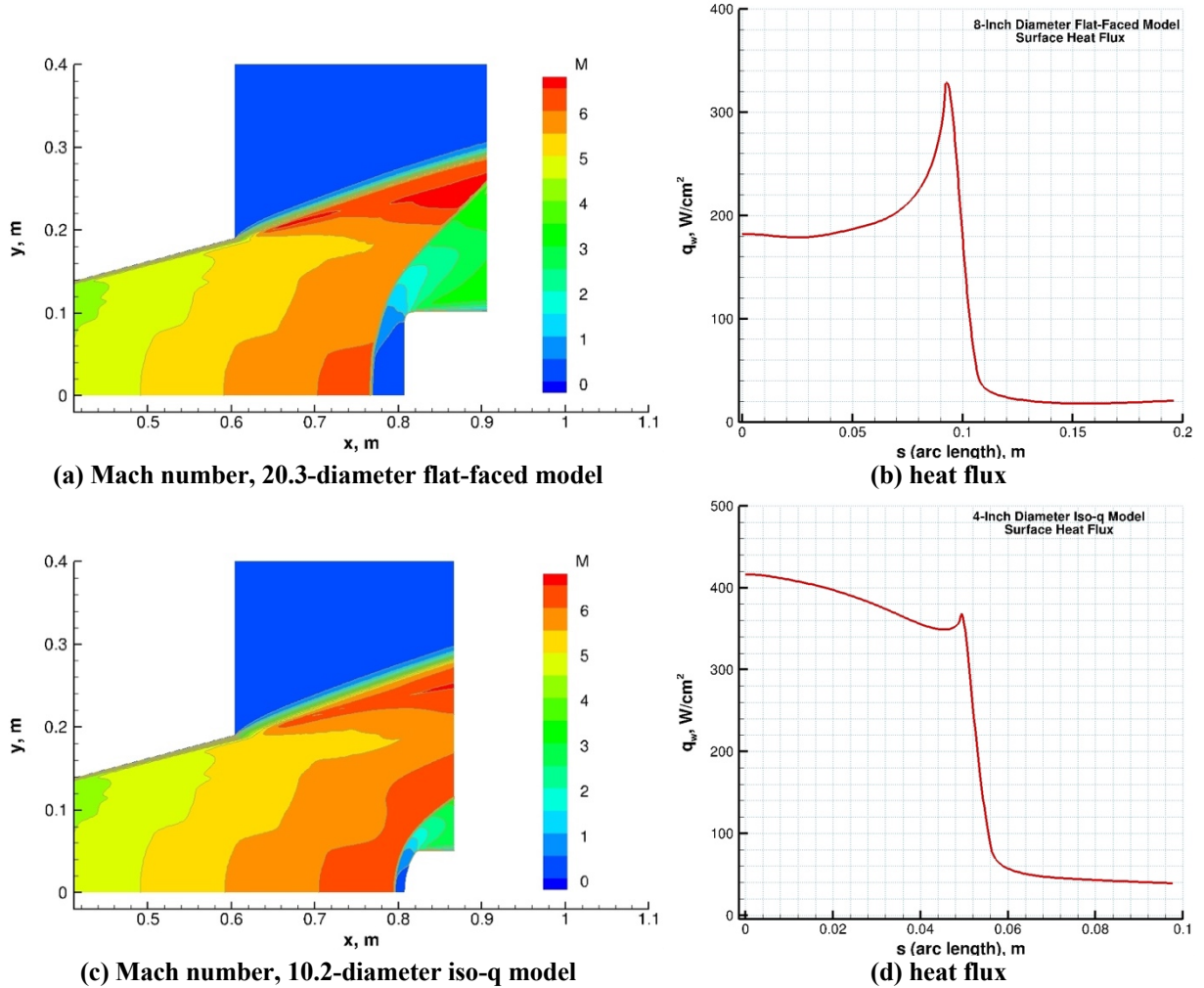


Figure 9. Computed Mach number contours and surface heat flux distributions of two calorimeter models. TP3 15-inch nozzle flow: $\dot{m} = 500$ g/s, $h_{ob} = 12.9$ MJ/kg, $h_{ocl} = 28.8$ MJ/kg, parabolic enthalpy profile, N_2/O_2 mixture, $p_{box} = 1$ torr.

As expected from the preceding discussion, the oblique shock wave formed near the throat reflects from the nozzle walls and eventually interacts with the model bow shock downstream at certain model locations. For some cases, this interaction is concern because it affects surface pressure and heating distributions on the model. Figure 9 shows computed Mach number contours and surface heat flux distributions of two calorimeter models: 20.3-cm flat-faced model and 10.2-cm iso-q model. For both cases, the oblique shock wave from the nozzle wall interacts with the model shock wave. Because of this interaction, the inflection in the model shock wave in Fig. 9a is clearly seen. Although there is a similar interaction in Fig. 9b, its effect appears to be less pronounced in the computed shock wave shape (interaction beyond the sonic point). The fact that surface heating distributions for both models appear to be typical of these model geometries is somewhat misleading, so the effects of the wave interactions on both model surface heat fluxes are not obvious. Note that the ratio of stagnation-point heat fluxes for these two models, q_{isoq}/q_{ffc8} , should be about 1.7 with ideal uniform freestream conditions, but for this case the ratio is 2.27. For this case, the effect of the flow disturbance on surface heat flux for the iso-q model is more than that for the flat-faced model. It should also be noted that the heating increase near the shoulder of the flat-faced model is quite significant, due to the model shock wave/flow disturbance interaction (the bow shock is pulled towards the body downstream).

There are two important implications of this interaction for arc-jet testing. First, the flow disturbance affects these model shock waves differently, so surface heat flux values and distributions for both models do not follow theoretically expected trends. The ratios of measured 10.2-cm iso-q and 20.3-cm flat-faced calorimeter heat fluxes become not consistent with analytical predictions (or CFD predictions when the flow disturbance is not accurately captured). In other words, one cannot estimate surface heat flux of the 20.3-cm flat-faced model from 10.2-cm iso-q calorimeter measurements. Second, because of this interaction, model surface heat flux distributions become very sensitive to the model location from the nozzle exit and facility conditions. As a result, calibration run anomalies occur, such as calorimeter measurements not being repeatable or being higher than expected for given arc current and mass flow rate. These effects of the flow disturbance on stagnation calorimeter models will also be presented in the next section.

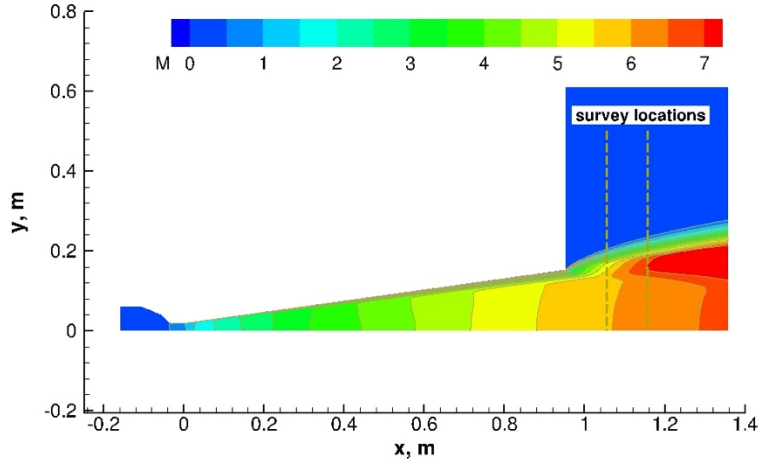
C. AHF 12-inch nozzle tests (AHF 345)

For this case, existence of a flow disturbance in the AHF 12-inch nozzle was also not known prior to the AHF 345 test series. During calibration runs using the flat-faced and iso-q calorimeters, several anomalies were observed, some of which are listed here: (1) facility repeatability issues (calorimeter measurements were not repeatable, and were sensitive to small changes in the arc heater conditions); (2) some of the measured calorimeter heat flux levels (both iso-q and flat-faced slugs) were much higher than expected for given arc current and mass flow rates; (3) the ratios of the iso-q and flat-faced calorimeter heat fluxes were not consistent with analytical or CFD predictions; (4) the measured heat fluxes did not follow an expected trend, a decreasing trend as the model moved further away from the nozzle exit. Although only one arc-jet condition listed in Table 1 is considered for the present paper, the mentioned anomalies were encountered for several arc-jet conditions in the AHF 345 tests. After several troubleshooting runs, 1.59-cm pitot pressure and Gardon gage probe sweeps were performed at $x_{ml} = 10.2$ cm and 20.3 cm locations (4 in and 8 in locations, potential model positions of interest for the test articles).

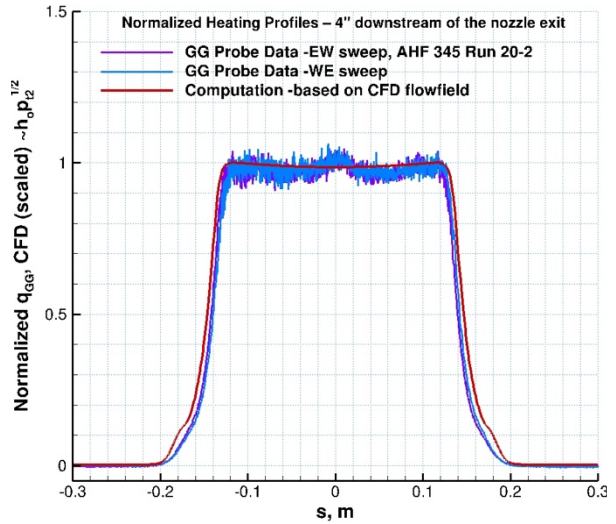
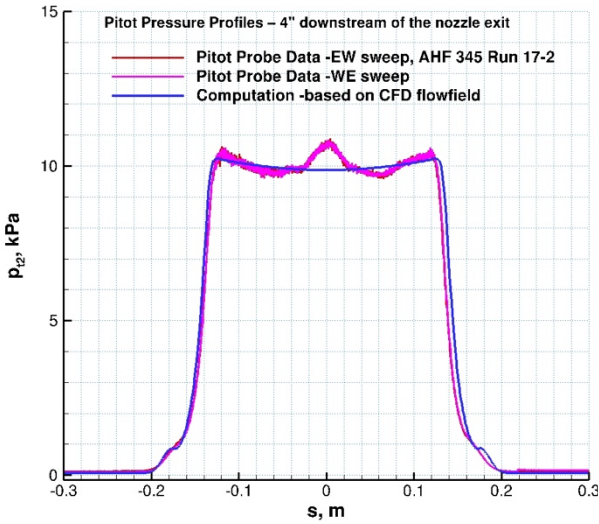
Figure 10 shows computed Mach number contours of the nozzle flow and test box, and comparisons of computations with the pitot pressure and Gardon-gage heat flux probe survey data at two axial locations. On the Mach number contour plot, the two axial probe survey locations are indicated. Both pitot pressure and heat flux data show a feature near the nozzle centerline at each axial location (Fig. 10 b and 10c), showing higher pressure and heating levels. Note that the features in the pressure data are more clearly detected than those in the heat flux data at both locations; and the feature is somewhat flattened at the 20.3 cm location. This feature is qualitatively similar to the one observed in the IHF 30-inch nozzle sweeps presented in Section A, which is an indication of a flow disturbance. Again, both pitot pressure and heat flux data are not exactly symmetric, but they are repeatable between two sweep directions (EW and WE). CFD-predicted pitot pressure and heat flux distributions are in reasonable agreement with the survey data except near the nozzle centerline. It should be noted here that the AHF 12-inch nozzle has an elongated throat like the TP3 15-inch nozzle, which results in a flow disturbance originating at the throat. However, this is much weaker than the one in the TP3 nozzle due to its throat design (the corner radius at the AHF throat and conical section intersection is much larger, see discussion on this in [5]). Nevertheless, this small disturbance can be observed in the Mach number contours shown in Fig. 10a. Typically, AHF CFD simulations show that the disturbance originating from the throat is more prominent at relatively low mass flow rates or when the test gas is N_2 .

In order to reproduce the measured survey data with CFD simulations, a flow disturbance in the nozzle (placed near the nozzle joint corresponding to the 7-inch nozzle exit, a 0.3 mm protuberance) is introduced. Again, the ultimate objective here is to investigate effects of the disturbance on the model surface quantities, while reproducing the measured sweep data. Figure 11 shows computed Mach number contours of the nozzle flow and test box, and comparisons of computations that included the flow disturbance with the pitot pressure and heat flux survey data. On the Mach number contour plot, the 7-inch nozzle exit location and axial survey locations are indicated. The introduced flow disturbance starts at about 0.5 m downstream of the throat as a compression wave and propagates downstream. Note that the pitot pressure survey data at both locations, to a lesser extent the heat flux data, are reasonably reproduced with these CFD simulations in Fig. 11b and 11c. It should be noted here that the strength of the pressure peak at $x_{ml} = 10.2$ cm location is less than the peak at the 20.3 cm location. As the flow disturbance propagates downstream, the peak near the centerline in fact flattens and turns into a dip at about $x_{ml} = 28$ cm location.

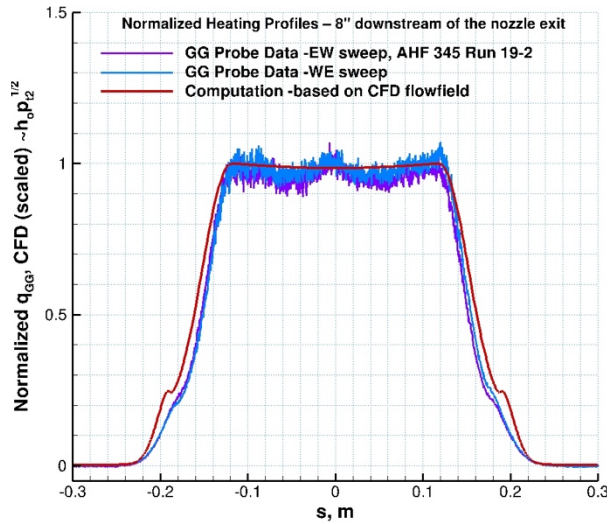
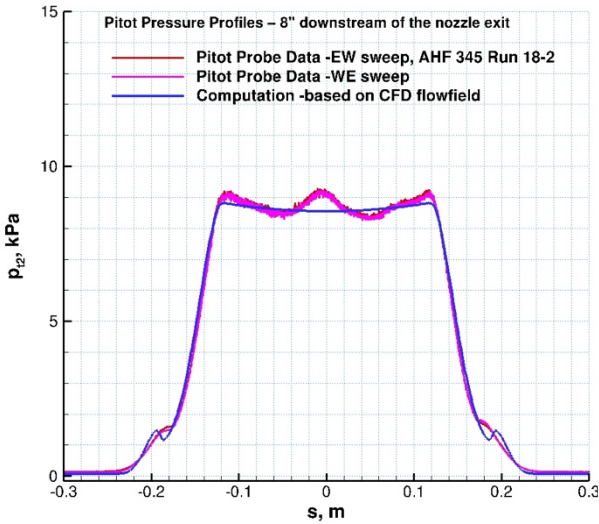
These sweeps and accompanying CFD analysis confirmed the existence of a flow disturbance in the AHF 12-inch nozzle flow during AHF 345 tests.



(a) Mach number contours

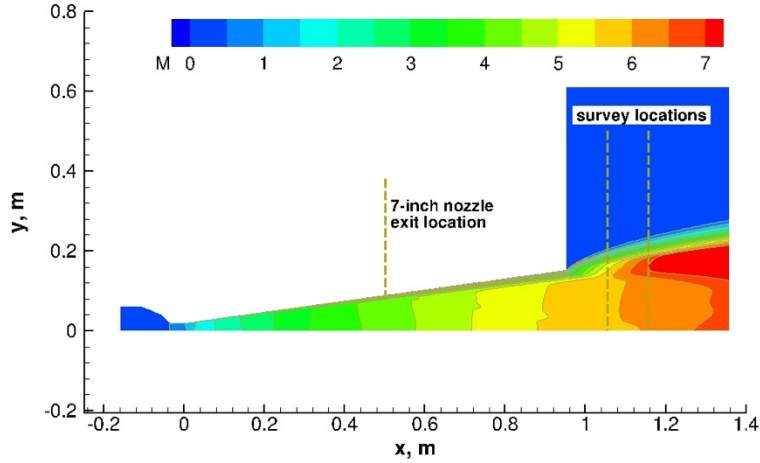


(b) probe sweeps at $x_{ml} = 10.2$ cm

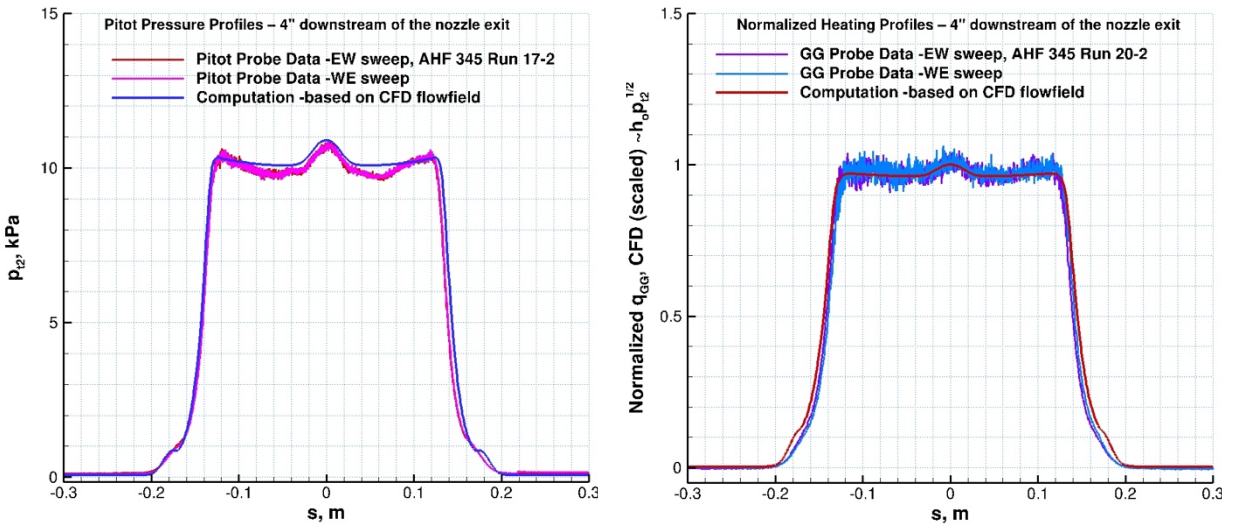


(c) probe sweeps at $x_{ml} = 20.3$ cm

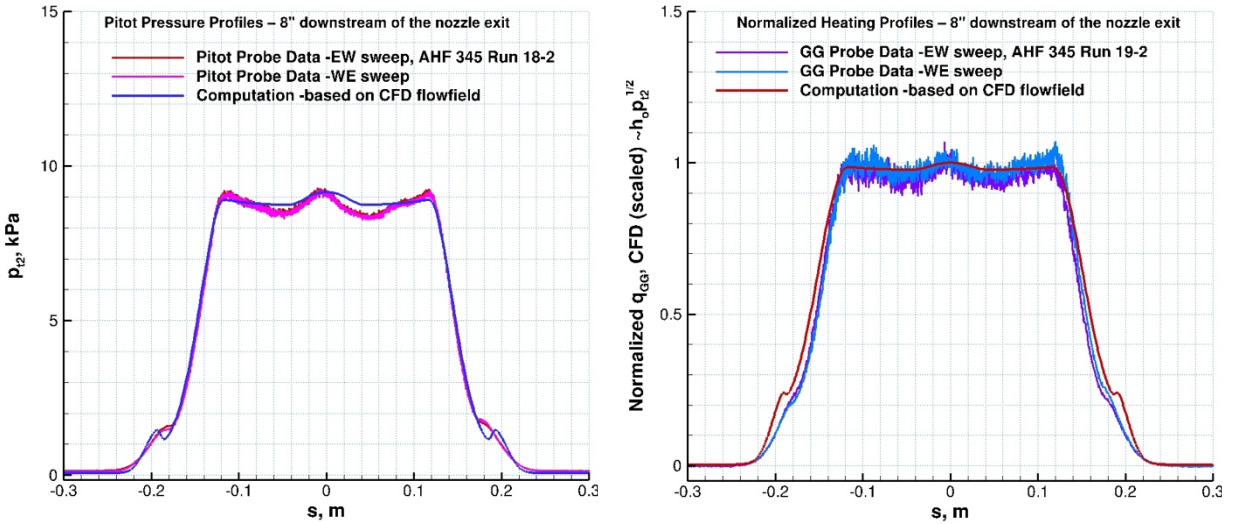
Figure 10. Computed Mach number contours and comparisons of computations with the pitot pressure and heat flux survey data at $x_{ml} = 10.2$ cm and 20.3 cm locations. AHF 12-inch nozzle flow: $\dot{m} = 185$ g/s, $h_{ob} = h_{oct} = 16.9$ MJ/kg, air with 8.1% Ar, $p_{box} = 0.5$ torr.



(a) Mach number contours



(b) probe sweeps at $x_{ml} = 10.2$ cm



(c) probe sweeps at $x_{ml} = 20.3$ cm

Figure 11. Computed Mach number contours and comparisons of computations including the flow disturbance with the pitot pressure and heat flux survey data at $x_{ml} = 10.2$ cm and 20.3 cm locations. AHF 12-inch nozzle flow: $\dot{m} = 185$ g/s, $h_{ob} = h_{oci} = 16.9$ MJ/kg, air with 8.1% Ar, $p_{box} = 0.5$ torr.

Figure 12 shows computed pressure contours near the nozzle exit, and comparisons of computed surface quantities of the 10.2-cm iso-q model at $x_{ml} = 10.2$ cm and 20.3 cm locations. In the pressure contours (Fig. 12a and 12b), the flow disturbance is clearly seen in both Fig. 12a and 12b as a compression wave followed by an expansion wave. The disturbance for each case interacts with the model bow shock wave at a different location, so effects of the interaction are naturally expected to be different for each case. Although the computed pressure contours are not presented for the nominal cases (undisturbed flow), computed model surface pressure and heat flux distributions are included here for comparison. As anticipated from the probe sweep data presented in Figs. 10 and 11, the flow disturbance increases the stagnation pressure on the models at both locations in comparison with the nominal cases. Note that the pressure distributions are still qualitatively similar, monotonically decreasing with arc length starting from the stagnation point. The effects on the heat flux distributions are much more complex. Depending on the location at which the disturbance and model bow shock intersects, different heat flux distributions are predicted. In comparison with the nominal cases, the predicted stagnation-point heat flux values are higher, but the decreasing trend in heat flux with the model location from the nozzle exit, x_{ml} , because of the drop in surface pressure, is no longer predicted.

Figure 13 shows computed pressure contours near the nozzle exit for the nominal case and one with the flow disturbance, and comparisons of computed surface quantities of the 10.2-cm iso-q model at $x_{ml} = 34.3$ cm location. As can be anticipated from the pressure contours in Fig. 13b, the effects of the disturbance on the model flowfield and surface quantities are relatively small at this location. Although one might consider testing at this location to reduce the effects of the flow disturbance, this is only a viable option at this condition or similar conditions for this model geometry. Interaction locations of the flow disturbance with the model flowfield vary with the arc-jet conditions, and flowfields of larger-sized models or different model geometries are affected differently.

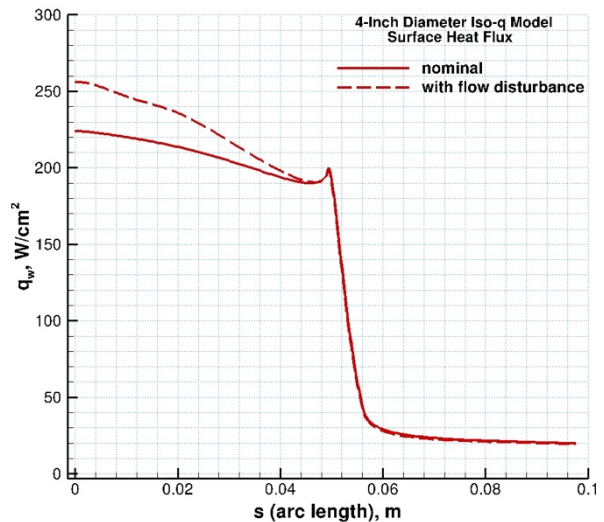
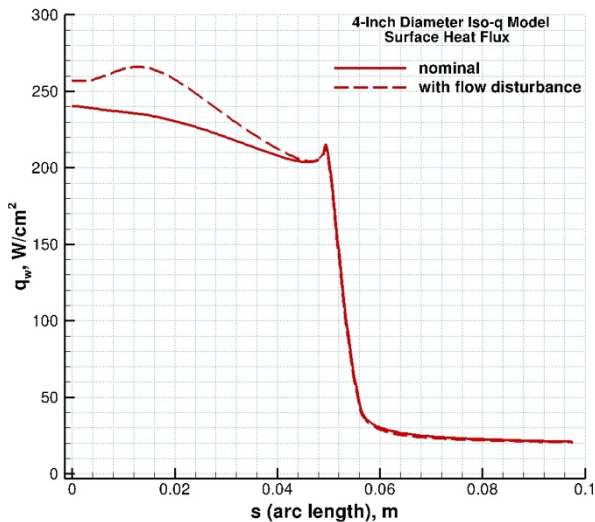
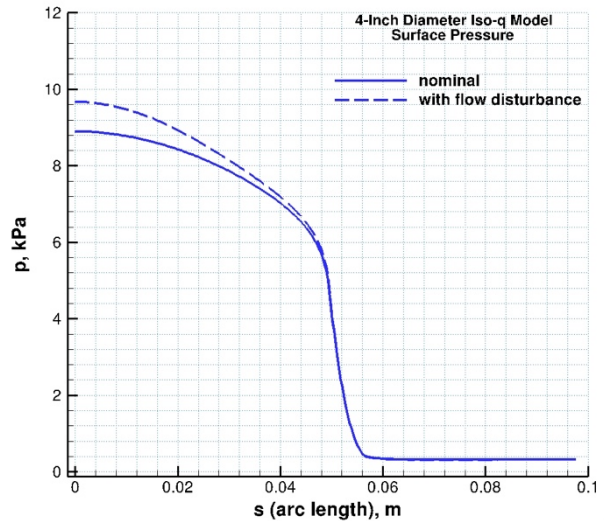
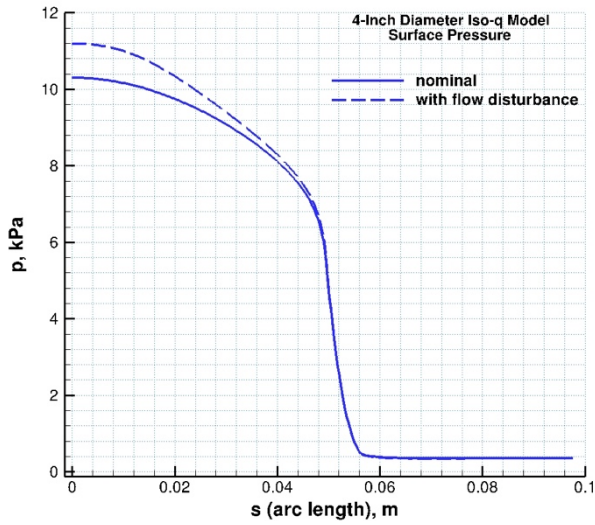
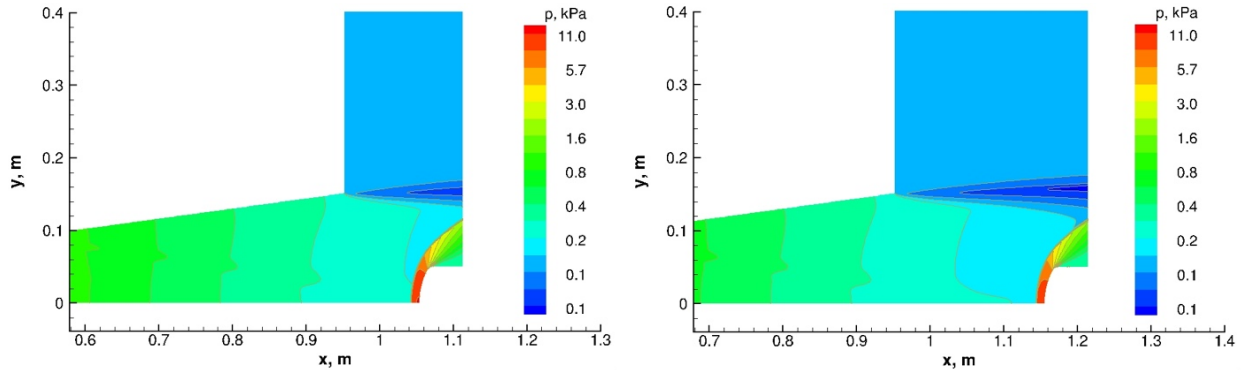
Figure 14 shows computed Mach number contours near the nozzle exit for the nominal case and one with the flow disturbance, and comparisons of computed surface quantities of the 20.3-cm flat-faced model at $x_{ml} = 20.3$ cm location. For this case the flow disturbance interacts with the model bow shock wave at a location upstream of the sonic line in the shock layer, as seen in Fig. 14b. As for its effects on the model surface quantities (Fig. 14c and 14d): in comparison with the nominal case, the surface pressure at the stagnation point has increased as expected, but its effects on the surface heating distribution is more dramatic. It should be noted that when the flow disturbance intersects with the subsonic portion of the bow shock wave (almost a normal shock wave), the disturbance effects resemble a type of shock-shock interaction, and the computed heat values become sensitive to the interaction location.

The CFD results shown in Figs. 12–14 qualitatively explain most of the mentioned calorimeter anomalies encountered in AHF 345 tests. The key to understanding of these anomalies is the existence of the flow disturbance in the test flow evidenced by the probe survey data and accompanying CFD analysis.

D. Computational grid details and estimated uncertainties

The two-dimensional axisymmetric and three-dimensional CFD computations of the IHF, TP3, and AHF nozzle flowfields, including the test box and models, were performed using multi-block grids. All computational grids were generated using a commercial software package, *Pointwise* [16]. Several different grids were used in the axisymmetric nozzle/test box simulations with and without stagnation calorimeter models. For the axisymmetric IHF 30-inch, TP3 15-inch, and AHF 12-inch nozzle simulations, the number of cells from the nozzle inlet to the nozzle exit were typically 640, 540, and 600 respectively (additional 180 to 240 cells in the test box), with 120 cells normal to the wall along the nozzle and 240 cells along the test box. For the three-dimensional IHF 30-inch nozzle/test box flowfields, 16.85 million cells were used. For the 10°-yawed wedge model flowfield simulations, the grid size was 4.75 million cells. Based on a limited number of grid refinement studies, grid quality issues of the computations and numerical accuracy are adequately addressed.

CFD computations of arc-jet flows, as for hypersonic flight simulations, include uncertainties in many of the model input parameters. It is not possible currently to do a complete uncertainty analysis of computed results for all the simulation input parameters. The most important input parameter of the arc-jet test flow is the total enthalpy and its distribution at the nozzle inlet. Noting that the centerline total enthalpies used in CFD simulations rely on slug calorimeter data, facility data, and other modeling input parameters, the uncertainty in heat flux predictions is estimated to be as much as $\pm 20\%$. The uncertainty in surface pressure predictions is estimated to be $\pm 5\text{--}10\%$.



(a) model at $x_{ml} = 10.2$ cm

(b) model at $x_{ml} = 20.3$ cm

Figure 12. Computed pressure contours near the nozzle exit and comparisons of computed surface quantities of the 10.2-cm iso-q model at $x_{ml} = 10.2$ cm and 20.3 cm locations, showing the effects of the flow disturbance. AHF 12-inch nozzle flow: $\dot{m} = 185$ g/s, $h_{ob} = h_{oct} = 16.9$ MJ/kg, air with 8.1% Ar, $p_{box} = 1$ torr.

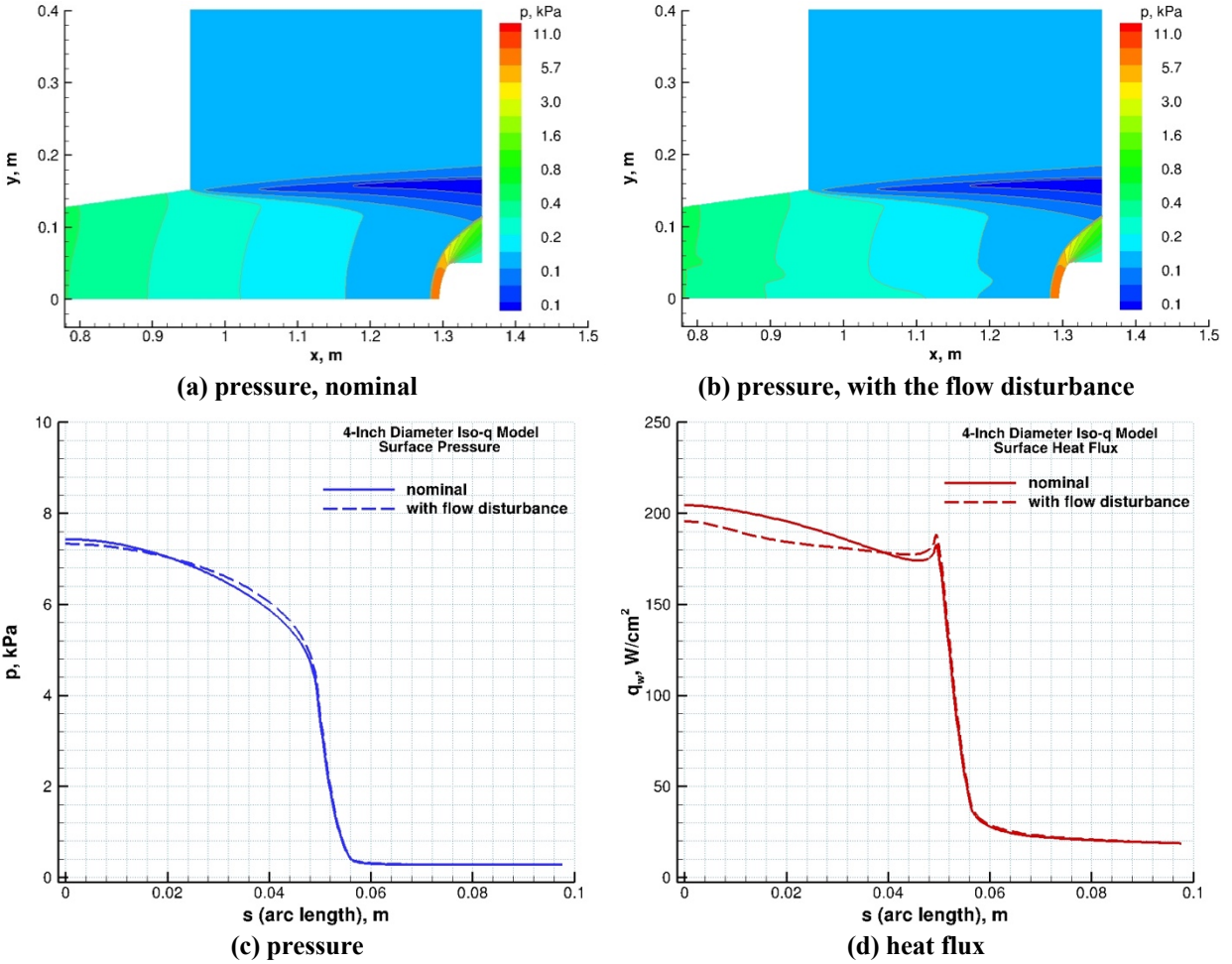


Figure 13. Computed pressure contours near the nozzle exit and comparisons of computed surface quantities of the 10.2-cm iso-q model at $x_{ml} = 34.3$ cm location, showing the effects of the flow disturbance. AHF 12-inch nozzle flow: $\dot{m} = 185$ g/s, $h_{ob} = h_{ocl} = 16.9$ MJ/kg, air with 8.1% Ar, $p_{box} = 1$ torr.

A complete uncertainty analysis of the heat flux and pressure measurements is not available. The slug calorimeter measurements [17] are standard facility measurements; based on historical NASA Ames arc-jet data with similar measurements, the slug heat flux measurements are estimated to be accurate to within $\pm 15\%$, and the pressure measurements to within $\pm 5\%$. Gardon-gage calorimeters [18] and the calorimeters with a coaxial thermocouple [19] are also frequently used in arc-jet testing. Although their estimated uncertainties are similar to that of the slug measurements, they could be larger especially when the probe sizes are relatively small. For the present work, the heat flux measurements from the 1.59-cm Gardon-gage probes in the TP3 and AHF nozzles, and from the 10.16-cm coaxial thermocouple calorimeter in the IHF 30-inch nozzle are used as qualitative measurements to provide normalized distributions of heat flux in the jet.

VI. Summary and Concluding Remarks

Computational simulations and analysis of flow characterization tests conducted in the NASA Ames arc-jet facilities are reported. The flow disturbances and their characterization are presented through three case studies: one in the 60-MW IHF 30-inch conical nozzle, one in the 10-MW TP3 15-inch conical nozzle, and another in the 20-MW AHF 12-inch conical nozzle. The test data included heat flux and pressure measurements with stagnation calorimeters, and surveys of arc-jet test flow with pitot pressure and heat flux probes. For each case, the survey probes are much smaller in size than the nozzle exit diameter, which is necessary to obtain spatial distributions of the pitot pressure and heat flux in the jet.

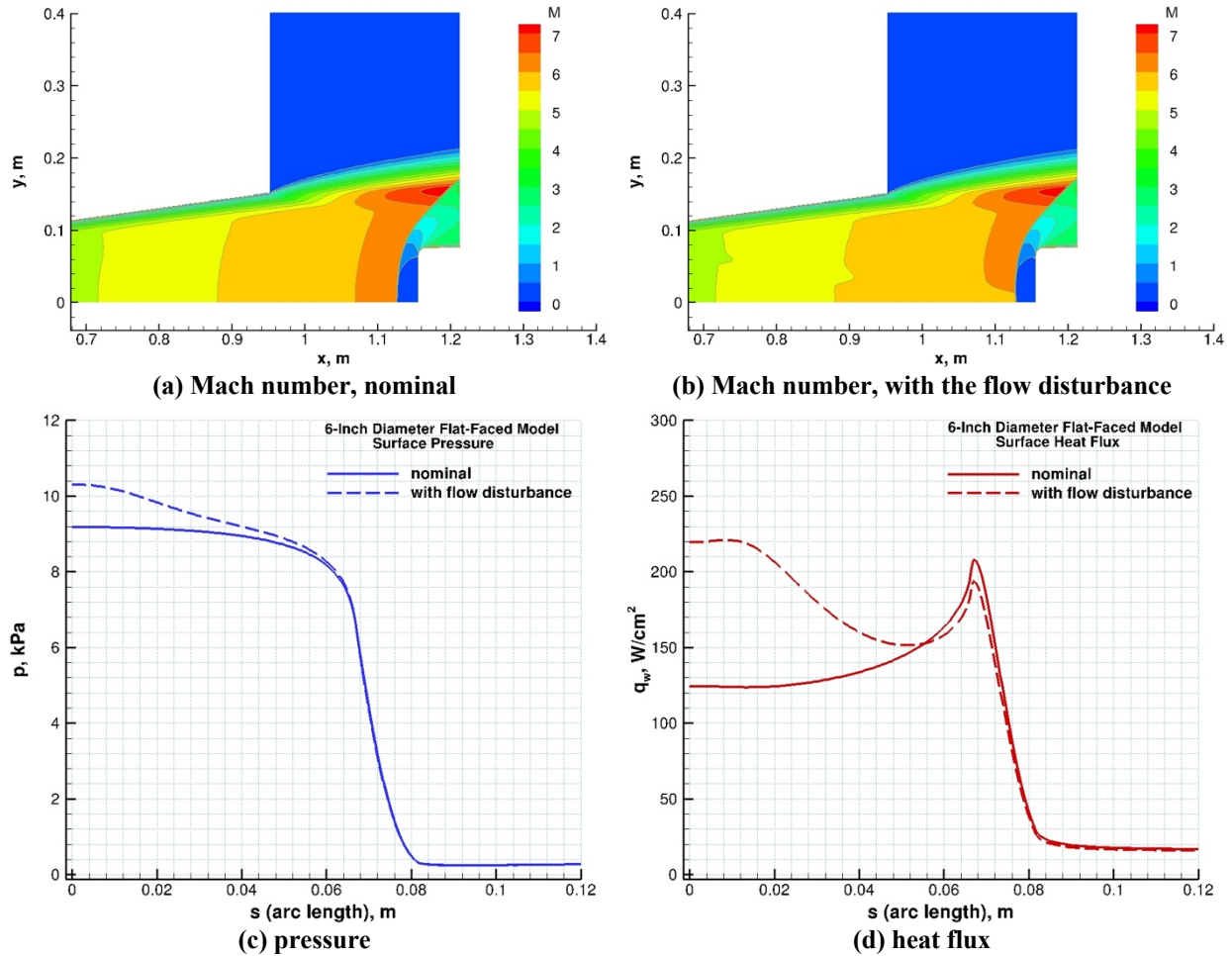


Figure 14. Computed Mach number contours near the nozzle exit and comparisons of computed surface quantities of the 15.2-cm flat-faced model at $x_{ml} = 20.3$ cm location, showing the effects of the flow disturbance. AHF 12-inch nozzle flow: $\dot{m} = 185$ g/s, $h_{ob} = h_{ocl} = 16.9$ MJ/kg, air with 8.1% Ar, $p_{box} = 1$ torr.

The present analysis comprises CFD simulations of the nonequilibrium flowfield in the facility nozzle and test box, including the models tested. Comparisons of computations with the experimental measurements in three arc-jet nozzles with different arc heaters are presented, showing reasonably good agreement. The computations that reproduce the probe sweep data approximately are used to explain experimental observations and calorimeter anomalies (e.g., dependence of the surface heat flux and pressure to model location and its unexpected sensitivity, the ratio of the iso- q and flat-faced calorimeter heat fluxes). These case studies show that the pitot pressure sweeps are especially important to detect any flow disturbance in the test flow. If there is a flow disturbance in the test flow and it is not detected, interpretation of both calorimeter and test data becomes difficult or inaccurate.

The probe sweeps are not routinely performed in arc-jet testing due to additional cost. However, these three case studies presented strongly suggest that they should be part of all arc-jet tests, noting that accurate interpretation of the arc-jet data requires well-characterized test environment. These probe sweeps play two important roles: (1) they provide an assessment of the flow non-uniformity and are used to set the inlet boundary conditions in CFD simulations (total enthalpy distribution based the sweep data); (2) as shown in these three case studies, they are critically important to detect any flow disturbance in the test flow.

Acknowledgments

The author would like to thank several people involved in three arc-jet test series: PIs for IHF 329 tests, David Stewart, and Kristina Skokova; PIs for AHF 341 tests, Eric Espesito (Lockheed Martin), Antonella Alunni, Shahab Salehghaffari, and Jonathan Morgan; PIs for AHF 345 tests, Jonathan Morgan, and Brandon Oliver (JSC); and the

TSF test engineers, Enrique Carballo, Frank Hui, and Imelda Terrazas-Salinas. This work was partially funded by the NASA Orion TPS Insight/Oversight and HTRM TUFROC projects. The support from the NASA Ames Entry Systems and Technology Division, through contract NNA15BB15C to AMA, Inc., is gratefully acknowledged.

References

- [1] Terrazas-Salinas, I., and the staff of Thermophysics Facilities Branch, “Test Planning Guide for NASA Ames Research Center Arc-Jet Complex and Range Complex,” A029-9701-XM3 Rev. D, Entry Systems and Technology Division, NASA Ames Research Center, January 2018.
- [2] Fretter, E., “Interaction Heating Facility (IHF) Fact Sheet,” <http://www.nasa.gov/centers/ames/thermophysics-facilities-home>, Thermophysics Facilities Branch, Entry Systems and Technology Division, NASA Ames Research Center, Sept. 2016.
- [3] Balboni, J. A., Gökçen, T., Hui, F. C. L., Graube, P., Morrissey, P., Lewis, R. “Consolidating NASA’s Arc-Jets,” AIAA Paper 2015-2667, June 2015.
- [4] Gökçen, T., Balboni, J. A., and Alunni, A. I. “Computational Simulations of the 10-MW TP3 Arc-Jet Facility,” AIAA Paper 2015-3103, June 2015.
- [5] Gökçen, T., “Analysis of Probe Surveys Conducted in the 10-MW TP3 Arc-Jet Facility 15-Inch Nozzle Flow,” AIAA Paper 2021-3149, June 2021.
- [6] Driver, D. M., Hartman, J., Philippidis, D., Noyes, E., Hui, F., and Terrazas-Salinas, I., “Evidence of Standing Waves in Arc Jet Nozzle Flow,” AIAA Paper 2017-4452, June 2017.
- [7] Terrazas-Salinas, I., Carballo, J. E., Driver, D. M., and Balboni, J. A., “Comparison of Heat Transfer Measurement Devices in Arc Jet Flows with Shear,” AIAA Paper 2010-5053, June 2010.
- [8] Wright, M. J., Candler, G. V., and Bose, D., “Data-Parallel Line Relaxation Method for the Navier-Stokes Equations,” *AIAA Journal*, Vol. 36, No. 9, 1998, pp. 1603-1609.
- [9] Wright, M. J., “Data-Parallel Line Relaxation Code, DPLR Version 4.02,” Private Communication, June 2010.
- [10] Park, C., *Nonequilibrium Hypersonic Aerothermodynamics*, John Wiley & Sons, Inc., New York, 1990, Chap. 4.
- [11] Gökçen, T., Chen, Y. K., Skokova, K. A., and Milos, F. S., “Computational Analysis of Arc-Jet Stagnation Tests Including Ablation and Shape Change,” *Journal of Thermophysics and Heat Transfer*, Vol. 24, No. 4, 2010, pp. 694-707; also, AIAA Paper 2009-3596, June 2009.
- [12] Gökçen, T., “Effects of Test Box Pressure on Arc-Jet Flowfields and Implications for Testing,” AIAA Paper 2018-3771, June 2018.
- [13] Gökçen, T., and Alunni, A. I., “CFD Simulations of the IHF Arc-Jet Flow: 9-Inch Nozzle, Flow Surveys, LEAF Wedge Calibration Data,” AIAA Paper 2019-3008, June 2019.
- [14] Gökçen, T., Boghazian, T., and Alunni, A. I., “CFD Simulations of the IHF 13-Inch Nozzle Flow: 55° Sphere-Cone Model, Manufactured Fences and Gaps,” AIAA Paper 2023-2427, January 2023.
- [15] Stewart, D. A., “Surface Catalysis and Characterization of Proposed Candidate TPS for Access-to-Space Vehicles,” NASA TM-112206, July 1997.
- [16] “*Pointwise*, Version 18.4,” Pointwise, Inc. of Cadence Design Systems, Fort Worth, TX.
- [17] ASTM E457-96, “Standard Test Method for Measuring Heat-Transfer Rate Using a Thermal Capacitance (Slug Calorimeter),” American Society for Testing and Materials, October 1996 (Reapproved 2002, originally published in 1972).
- [18] ASTM E511-07, “Standard Test Method for Measuring Heat Flux Using a Copper-Constantan Circular Foil Heat-Flux Gage,” American Society for Testing and Materials, December 2007 (original standard published in 1973).
- [19] Driver, D. M., Philippidis, D., and Terrazas-Salinas, I., “Uncertainty Analysis of Coaxial Thermocouple Calorimeters used in Arc Jets,” AIAA Paper 2018-3770, June 2018.